

LBGrain: An efficient multiscale lattice Boltzmann model for granular flows

Y.J. Huang¹, T. Wang², G.C. Yang^{1,*}, L. Jing³, C.Y. Kwok², and Y.D. Sobral⁴

¹School of Aeronautics and Astronautics, Sun Yat-sen University, Guangzhou, PR China

²Department of Civil Engineering, The University of Hong Kong, Haking Wong Building, Pokfulam Road, Hong Kong, PR China

³Institute for Ocean Engineering, Shenzhen International Graduate School, Tsinghua University, Shenzhen, China

⁴Departamento de Matemática, Universidade de Brasília, Campus Universitário Darcy Ribeiro, 70910-900 Brasília DF, Brazil

Abstract. We incorporate the Navier slip boundary condition into LBGrain, a multiscale lattice Boltzmann framework for granular flows, and validate its performance through comparisons with discrete element method (DEM) simulations. Rheological parameters of the granular flows are extracted from the coarse-grained results based on DEM data. Granular assemblies are treated as viscoplastic fluids, with their apparent viscosity governed by the regularized $\mu(I)$ rheology. A single-phase free-surface model is employed to track the fluid-gas interface. Navier slip boundary condition is introduced to quantify the basal slip of granular flows. Numerical validation of LBGrain is conducted through simulations of the periodic chute flow on an inclined plane, comparing with the reference data obtained from DEM. Results demonstrate an excellent agreement between the LBGrain velocity profiles and the theoretical Bagnold profiles extracted from the DEM data under varying inclination angles and flow depths, proving the accuracy of LBGrain.

1 Introduction

Multiscale modeling of granular flows is a critical research frontier in bridging macroscopic phenomena with microscopic physical mechanisms, facilitating efficient continuum modeling of granular media. The $\mu(I)$ rheology [1] captures the non-Newtonian behavior of granular flows, and now various models [2–5] have extended this framework, providing theoretical fundamentals of the continuum modeling and simulation of the dense granular flows. In continuum approaches, granular materials are treated as viscoplastic fluids governed by appropriate constitutive relationships, and simulated by computational fluid dynamics (CFD). This strategy has been successfully implemented across varying CFD techniques, including classical Eulerian CFD [6, 7] as well as modern CFD methods such as MPM [8], SPH [9], LBM [10, 11], etc.

Boundary conditions represent another critical component in continuum modeling, as they simplify intricate particle-boundary interactions into macroscopic approximations. The conventional boundary schemes for granular flow continuum include no-slip [6–8, 10] and Coulomb frictional boundary conditions [9, 11]. Notably, the Navier slip scaling law for basal slip in granular flows is proposed by Artoni *et al.* [12], which has been confirmed both experimentally [13] and numerically [12, 14], offering a novel insight for understanding and modeling the boundary behavior of granular flows. The Navier slip boundary is well established in CFD, but its integration into continuum modeling of granular flows remains relatively underexplored [15].

In the paper, we implement the Navier slip boundary condition into LBGrain [10, 11] – a multiscale lattice Boltzmann framework for granular flows. Section 2 outlines methodologies briefly. Section 3 tests the performance of LBGrain through the comparison of numerical results from the LBM and DEM simulations of the periodic chute flow on an inclined plane. Section 4 summarizes our work.

2 LBGrain framework

2.1 Lattice Boltzmann method for free surface flows

The basic equation of lattice Boltzmann method (LBM) is

$$f_i(\mathbf{x} + \mathbf{c}_i \delta_t, t + \delta_t) - f_i(\mathbf{x}, t) = -\frac{1}{\tau} \left[f_i(\mathbf{x}, t) - f_i^{(\text{eq})}(\mathbf{x}, t) \right] + F_i, \quad (1)$$

where $f_i(\mathbf{x}, t)$ represents the density distribution function at (\mathbf{x}, t) along the direction \mathbf{c}_i , δ_t is the time step, τ is the relaxation time in LBM, $f_i^{(\text{eq})}$ is the Maxwellian equilibrium distribution function [16], $F_i = w_i \rho (\mathbf{c}_i \cdot \mathbf{a}) / c_s^2$ is the source term [16], \mathbf{a} is the acceleration of external force, ρ is fluid density. For two-dimensional simulations, the D2Q9 velocity model [17] is employed in Eq. 1, where the lattice sound speed is $c_s = 1/\sqrt{3}$. The fluid dynamic viscosity η is

$$\eta = \rho c_s^2 \left(\tau - \frac{1}{2} \right) \delta_t. \quad (2)$$

Macroscopic hydrodynamic quantities are obtained by $\rho = \sum_i f_i$, $\rho \mathbf{u} = \sum_i f_i \mathbf{c}_i$, and $p = \rho c_s^2$, where the \mathbf{u} and p are fluid velocity and pressure, respectively.

*e-mail: yanggch8@mail.sysu.edu.cn

A single-phase free surface model based on Volume-of-Fluid method [18, 19] is adopted to capture fluid-gas interface with simplicity and efficiency. The free surface boundary condition between the interface cell at \mathbf{x} and the gas cell at $\mathbf{x} + \mathbf{c}_i \delta_t$ is defined based on the non-equilibrium bounceback scheme, i.e.,

$$f_{-i}(\mathbf{x}, t + \delta_t) = f_i^{(eq)}(\rho_A, \mathbf{u}(\mathbf{x})) + f_{-i}^{(eq)}(\rho_A, \mathbf{u}(\mathbf{x})) - f_i(\mathbf{x}, t), \quad (3)$$

where $\rho_A = 1$ is the density of gas cell, and subscript $-i$ denotes the direction $\mathbf{c}_{-i} = -\mathbf{c}_i$. Details of mass exchange and cell update schemes can be found in [19].

2.2 Rheology of dense granular flows

Friction coefficient μ is the ratio of shear stress σ to normal pressure p , and it is related to the inertial number I . Jop *et al.* [2] proposed $\mu(I)$ rheology as

$$\mu(I) = \frac{\sigma}{p} = \mu_s + \frac{\mu_d - \mu_s}{I_0 + I}, \quad \text{with } I = \dot{\gamma} d_p / \sqrt{p/\rho_p}, \quad (4)$$

where μ_s, μ_d and I_0 are model parameters, ρ_p is the particle density, d_p is the particle diameter, $\gamma_{ij} = \frac{1}{2} \left(\frac{\partial u_i}{\partial x_j} + \frac{\partial u_j}{\partial x_i} \right)$ is the strain rate tensor, and $\dot{\gamma} = \sqrt{2\gamma_{ij}\gamma_{ij}}$ is the shear rate.

The apparent dynamic viscosity of the equivalent continuum is $\eta = \mu(I)p/\dot{\gamma}$. To mitigate numerical singularity when $\dot{\gamma}$ approaches 0, the regularized η is written as Eq. 5,

$$\eta_{app} = \frac{\mu_s p}{\dot{\gamma}} \left(1 - \exp\left(-\frac{\dot{\gamma}}{\lambda}\right) \right) + \frac{(\mu_d - \mu_s) p d_p}{I_0 \sqrt{p/\rho_p} + \dot{\gamma} d_p}, \quad (5)$$

where $\lambda = 0.1 \text{ s}^{-1}$ is the regularization parameter [10]. To ensure numerical stability in regions approaching free surfaces, we impose a minimum pressure threshold $p_{\min} = \rho_p g d_p$ for non-gas computational nodes in which $p \leq 0$. The p_{\min} corresponds to the hydrostatic pressure exerted by a single particle layer above the free surface.

In LBM, the shear rate magnitude $\dot{\gamma}$ is computed by local second-order velocity moment of non-equilibrium distribution functions [20],

$$\Pi_{\alpha\beta}^{(neq)} = \sum_i c_{i\alpha} c_{i\beta} (f_i - f_i^{(eq)}) = -2c_s^2 \rho \tau \gamma_{\alpha\beta}. \quad (6)$$

Prior to advancing to time step $t + \delta_t$, we calculate $\dot{\gamma}(t)$ using Eq. 6 with the current relaxation time $\tau(t)$. Then we apply $\dot{\gamma}(t)$ in Eq. 5 for obtaining $\eta_{app}(t + \delta_t)$. Finally, the $\eta_{app}(t + \delta_t)$ is used in Eq. 2 to determine $\tau(t + \delta_t)$ locally.

2.3 Navier slip boundary condition

Implementing Navier slip boundary in LBM requires reconstruction of unknown distribution functions. The Navier slip length is denoted by l_s in Fig. 1(a), and fluid slip velocity is defined as $u_{\text{slip}} = l_s \left. \frac{\partial u_x}{\partial y} \right|_{y=0}$. Fig. 1(b) illustrates the corresponding LBM representation, where $f_{\nearrow}(\mathbf{x}_f)$ is unknown since $f_{\nearrow}(\mathbf{x}_s)$ is undefined at the solid node. The reconstruction of $f_{\nearrow}(\mathbf{x}_f)$ is the weighted average of both no-slip and free-slip bouncebacks [21], i.e.,

$$f_{\nearrow}(\mathbf{x}_f) = s_c \underbrace{f_{\nearrow}(\mathbf{x}_{\bar{f}})}_{\text{free-slip}} + (1 - s_c) \underbrace{f_{\nearrow}(\mathbf{x}_f)}_{\text{no-slip}}, \quad (7)$$

where $s_c \in [0, 1]$ represents the slip coefficient in LBM, \mathbf{c}_{\searrow} is the mirror symmetric vector of \mathbf{c}_{\nearrow} with respect to the wall. The relationship between s_c and l_s is given by $l_s = \left(\tau - \frac{1}{2} \right) \frac{s_c}{1 - s_c}$ as reported in [22]. For straight boundaries, the scheme's advantage lies in preserving local mass conservation in LBM by substituting $f_{\searrow}(\mathbf{x}_{\bar{f}})$ with $f_{\searrow}(\mathbf{x}_f)$.

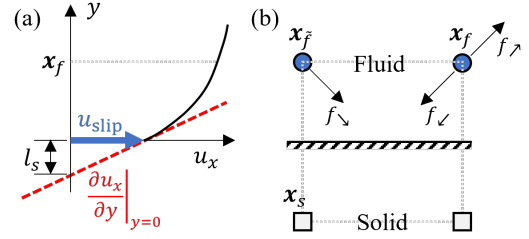


Figure 1. Sketch of (a) straight Navier slip boundary, and (b) corresponding LBM distribution functions near the wall.

For continuum simulation via LBGrain, rheological parameters and Navier slip length l_s should be obtained from coarse-grained DEM data or experimental results first. Then LBM simulations are performed with the measured rheological and boundary parameters. This general procedure is validated in Sec. 3.

3 Granular flow on an inclined plane

3.1 Discrete element simulation

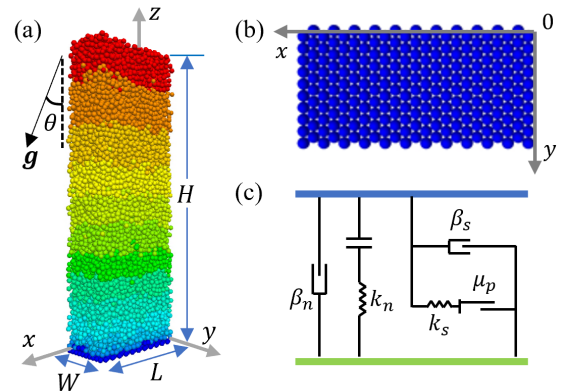


Figure 2. Sketch of DEM simulation: (a) geometric shape; (b) packing of basal particles; (c) Hertz contact model.

Dense granular flow on an inclined plane with a tilt angle θ is a commonly adopted benchmark test. The DEM simulation domain is shown as Fig. 2(a). Particles with density $\rho_p = 2650 \text{ kg/m}^3$ exhibit a uniform diameter distribution in $[0.9d_p, 1.1d_p]$, where $d_p = 1 \text{ mm}$ is the mean diameter. Chute dimensions are defined by length $L = 20d_p$, width $W = 10d_p$ and height H , with periodic boundaries imposed along x and y directions. A basal layer of fixed particles with diameters of $d_b = d_p$ is arranged in hexagonal close packing as shown in Fig. 2(b). Particle interactions are governed by the Hertz contact model (Fig. 2(c)), whose contact parameters are listed in Table 1. The shear stress and normal pressure are defined as stress component σ_{zx} and σ_{zz} respectively.

Assume that the solid volume fraction Φ is constant, and the basal Navier slip length is l_s . The theoretical friction coefficient across the field is $\mu = \tan \theta$. With the $\mu(I)$

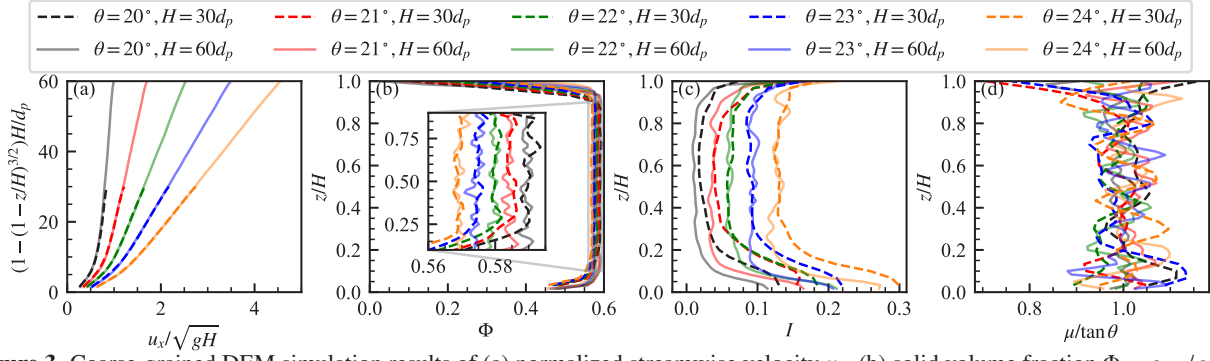


Figure 3. Coarse-grained DEM simulation results of (a) normalized streamwise velocity u_x , (b) solid volume fraction $\Phi = \rho_{CG}/\rho_p$, (c) inertial number I and (d) friction coefficient μ .

rheology in Eq. 4, the normalized streamwise velocity profile u_x along flow depth z is:

$$\frac{u_x(z)}{\sqrt{gH}} = \left[1 - \left(1 - \frac{z}{H} \right)^{3/2} \right] a + b \quad (8)$$

where $a = 2HI_\theta \sqrt{\Phi \cos \theta}/3d_p$, $b = 3al_s/2H$ and $I_\theta = (\tan \theta - \mu_s)I_0/(\mu_d - \tan \theta)$. The part $[1 - (1 - z/H)^{3/2}]$ is called Bagnold velocity profile.

Table 1. Contact parameters of particles in DEM simulation

Physical variable	Value
Young's modulus E	10^9 Pa
Possion's ratio ν	0.4
Friction coefficient μ_p	0.5
Normal critical damping ratio β_n	0.2
Shear critical damping ratio β_s	0.2

3.2 DEM results

Unlike Weinhart *et al.* [23, 24], which focus on the coarse graining methods, our DEM simulations employ a setup with specific particle properties and contact parameters tailored to validate LBGrain for granular flows on inclined planes. DEM simulations are conducted with $H = [30d_p, 60d_p]$ and $\theta \in [20^\circ, 21^\circ, 22^\circ, 23^\circ, 24^\circ]$, whose steady-state results are processed using the coarse graining method proposed by Weinhart *et al.* [23, 24]. Fig. 3(a) shows that the normalized streamwise velocity u_x profiles collapse onto the same curve for each θ . A distinct steeper flow regime occurs at $(1 - (1 - z/H)^{3/2})H/d_p \leq 10$, indicating boundary layer effects. In Fig. 3(b-c), Φ and I remain essentially stable within $z \in (0.3H, 0.8H)$ for fixed θ , while other trends occur near the free surface and boundary layer. Increasing θ enhances flow velocity, thereby elevating I while reducing Φ . In Fig. 3(d), μ is generally consistent with $\tan \theta$, validating the assumptions of Eq. 8. The constitutive relationships and their corresponding fitting curves are shown in Fig. 4. The $\mu(I)$ rheology is fitted by Eq. 4, yielding parameters $\mu_s = 0.353453$, $\mu_d = 1.169347$ and $I_0 = 1.037364$. For the $\Phi(I)$ relationship, we adopt the equation proposed by Da Cruz *et al.* [25], i.e., $\Phi(I) = \Phi_{\max} - \alpha I$, with fitting parameters $\Phi_{\max} = 0.590972$ and $\alpha = 0.171274$.

Fig. 5 compares the streamwise velocity of DEM results ($u_{x,CG}$) with Bagnold curves ($u_{x,B}$) fitted by Eq. 8, where the depth-averaged solid volume fraction $\bar{\Phi}_\theta$ at each

θ is substituted for Φ in Eq. 8. DEM results agree with Bagnold profiles above $z > 7d_p$, but exhibit steeper gradients below this threshold. Thus, Table 2 presents two length scales: $l_{s,D} = (u_{x,CG}/\frac{du_{x,CG}}{dz})_{z=0}$ denotes the Navier slip length that characterizes the local slip behavior at the actual flow-bed interface; and $l_B = (u_{x,B}/\frac{du_{x,B}}{dz})_{z=0}$ is the equivalent length scale quantifying the boundary velocity extrapolated from $u_{x,B}$. The $l_{s,D}$ exhibits an overall consistent positive correlation with θ , with convergence observed at higher θ across varying H . Conversely, l_B decreases significantly as θ increases, and only approximate the bulk flow regime above $z = 7d_p$ via Eq. 8. Given that Bagnold velocity profiles capture the bulk flow regime accurately, l_B is adopted for quantifying basal slip, and omit boundary layer effects intentionally.

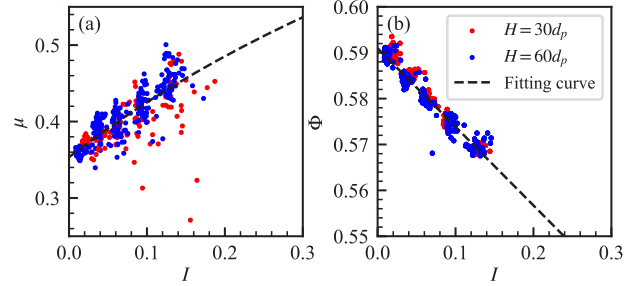


Figure 4. (a) $\mu(I)$ and (b) $\Phi(I)$ relationships based on DEM data. The dashed lines are fitting curves.

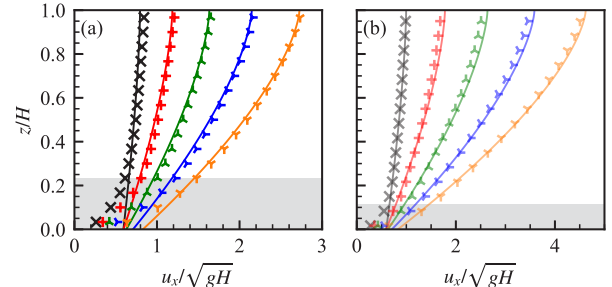


Figure 5. Streamwise velocity of DEM results ($u_{x,CG}$ in markers) and corresponding fitted Bagnold profiles ($u_{x,B}$ in solid lines with the same color) under (a) $H = 30d_p$ and (b) $H = 60d_p$. Height of gray areas are $7d_p$. Color scheme matches the legend in Fig. 3.

3.3 Accuracy and convergence of LBGrain

LBM simulation is performed based on the fitted rheological parameters extracted from Fig. 4. The two-dimensional domain replicates the geometry of the xOz -plane in Fig. 2(a), where x direction is periodic and Navier

Table 2. Length scales for quantifying basal slip in DEM results

θ	$\frac{l_{s,D}}{d_p} (H = 30d_p)$	$\frac{l_{s,D}}{d_p} (H = 60d_p)$	$\frac{l_B}{d_p}$
20°	1.914725	2.159804	58.859279
21°	2.214448	2.086445	20.006286
22°	2.110052	2.002792	12.510577
23°	2.284009	2.290093	9.862837
24°	2.389556	2.351891	8.747380

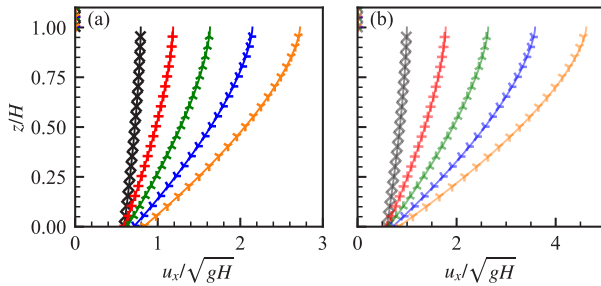


Figure 6. Streamwise velocity u_x of LBG grain results (markers) and theoretical Bagnold velocity (solid lines) under (a) $H = 30d_p$ and (b) $H = 60d_p$. Color scheme matches the legend in Fig. 3.

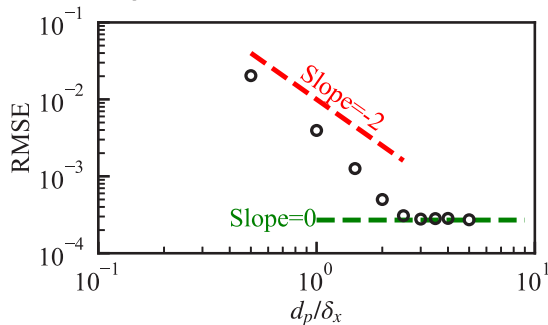


Figure 7. Root mean square error (RMSE) of velocity u_x between LBG grain result and analytical Bagnold solution.

slip boundary at $y = 0$. A layer of gas with the thickness of $0.1H$ is set above the free surface to validate the VOF method. The fluid density is $\rho_f(\theta) = \Phi(I_\theta)\rho_p$. The grid size is $\delta_x = d_p/4$, and the time step $\delta_t = \delta_x^2/(0.1 \text{ m}^2/\text{s})$ maintains $\delta_t \propto \delta_x^2$ relationship, thereby ensuring shear stress convergence in LBM. In Fig. 6, the LBM velocity profile u_x agrees with Bagnold's solution with less than 0.66% relative error, validating the capability of LBG grain to recover Eq. 8 from given rheological parameters. The vanishing velocity field ($u_x \equiv 0$) above $z = H$ confirms the stability of VOF method.

We further evaluated the numerical convergence of LBG grain by simulating a case with $\theta = 24^\circ$ and $H = 60d_p$ under varying $\delta_x = d_p/k$. The root mean square errors (RMSE) between LBG grain results and analytical solutions are shown in Fig. 7. The slope of RMSE approaches -2 with increasing k , confirming the second order accuracy of LBM. For $k \geq 3$, the accuracy is limited by the regularization term in Eq. 5, agreeing with [26].

4 Conclusions

This study incorporates the Navier slip boundary condition into LBG grain [10, 11], a multiscale lattice Boltzmann framework for granular flows. Numerical validation through periodic chute flow simulations demonstrates the capability of LBG grain to accurately reproduce the primary bulk flow regime observed in DEM reference data.

LBG grain advances the multiscale modeling and simulation of free-surface granular flows, with flexibility to update both constitutive relationships and boundary conditions. Considering the advantages of LBM in efficient parallelism and its simplicity in dealing with complex boundaries, LBG grain holds promising potential for solving large-scale granular flow problems with irregular topologies.

References

- [1] GDR MiDi, Eur. Phys. J. E **14**, 341 (2004).
- [2] P. Jop, Y. Forterre, O. Pouliquen, Nature **441**, 727 (2006).
- [3] O. Pouliquen, Y. Forterre, Phil. Trans. R. Soc. A **367**, 5091 (2009).
- [4] P. Jop, Comptes Rendus. Physique **16**, 62 (2015).
- [5] K. Kamrin, Front. Phys. **7**, 116 (2019).
- [6] D. Faroux, K. Washino, T. Tsuji, T. Tanaka, EPJ Web Conf. **249**, 03025 (2021).
- [7] P.Y. Lagrée, L. Staron, S. Popinet, J. Fluid Mech. **686**, 378 (2011).
- [8] S. Dunatunga, K. Kamrin, J. Fluid Mech. **940**, A14 (2022).
- [9] M. Kheirkhahan, P. Omidvar, P. Nikeghbali, P. Pasereh, S. Nayyer, Multiscale Multidiscip. Model. Exp. Des. (2024).
- [10] G.C. Yang, S.C. Yang, L. Jing, C. Kwok, Y. Sobral, J. Comput. Phys. **479**, 111956 (2023).
- [11] G.C. Yang, Y.J. Huang, Y. Lu, C.Y. Kwok, Y.D. Sobral, Q.H. Yao, J. Fluid Mech. **973**, A21 (2023).
- [12] R. Artoni, A.C. Santomaso, M. Go', P. Canu, Phys. Rev. Lett. **108**, 238002 (2012).
- [13] C.C. Lin, R. Artoni, F.L. Yang, P. Richard, J. Fluid Mech. **969**, A7 (2023).
- [14] R. Artoni, P. Richard, Phys. Rev. Lett. **115**, 158001 (2015).
- [15] R. Artoni, A. Santomaso, P. Canu, Chem. Eng. Sci. **64**, 4040 (2009).
- [16] X. He, Q. Zou, L.S. Luo, M. Dembo, J. Stat. Phys. **87**, 115 (1997).
- [17] Y.H. Qian, D. D'Humières, P. Lallemand, Europhys. Lett. **17**, 479 (1992).
- [18] C. Körner, M. Thies, T. Hofmann, N. Thürey, U. Rüde, J Stat Phys **121**, 179 (2005).
- [19] N. Thürey, C. Körner, U. Rüde, Technical Report 05-4. University of Erlangen-Nuremberg (2005).
- [20] S. Hou, J. Sterling, S. Chen, G. Doolen, Pattern formation and lattice gas automata **6**, 151 (1996).
- [21] S. Succi, Phys. Rev. Lett. **89**, 064502 (2002).
- [22] O. Švec, J. Skoček, J. Non-Newtonian Fluid Mech. **199**, 61 (2013).
- [23] T. Weinhart, A.R. Thornton, S. Luding, O. Bokhove, Granular Matter **14**, 531 (2012).
- [24] T. Weinhart, R. Hartkamp, A.R. Thornton, S. Luding, Phys. Fluids **25**, 070605 (2013).
- [25] F. Da Cruz, S. Emam, M. Prochnow, J.N. Roux, F. Chevoir, Phys. Rev. E **72**, 021309 (2005).
- [26] E. Mitsoulis, Th. Zisis, J. Non-Newtonian Fluid Mech. **101**, 173 (2001).